

---

**RESEARCH ARTICLE**

# Impact of Small-Scale Gravity Waves on Tracer Transport

Irmgard Knop<sup>1</sup> | Stamen Dolaptchiev<sup>1</sup> | Ulrich Achatz<sup>1</sup>

<sup>1</sup>Institute for Atmosphere and Environment,  
Goethe University Frankfurt, Germany

**Correspondence**

Irmgard Knop, Institute for Atmosphere and Environment, Goethe University Frankfurt, Altenhöferallee 1, D-60438 Frankfurt am Main, Germany  
Email: knop@iau.uni-frankfurt.de

**Funding information**

Deutsche Forschungsgemeinschaft,  
Grant/Award Number: 428312742,  
274762653

**Abstract**

Small-scale gravity waves play a crucial role in atmospheric tracer transport, yet their effects remain unresolved in climate models and must be parameterized. This study investigates how gravity waves influence large-scale tracer distributions, utilizing a multiple-scale analysis to systematically identify the governing terms of gravity wave-induced tracer fluxes. The analysis reveals both leading-order and next-order impacts: the former being the inertia-gravity wave-induced tracer Stokes drift, which acts perpendicular to both the large-scale tracer gradient and the wave number, while the latter becomes significant at lower latitudes where Coriolis effects diminish. A numerical framework is developed to incorporate these fluxes into a gravity wave parameterization model, potentially enhancing climate model accuracy without requiring explicit resolution of small-scale wave dynamics. Model validation against high-resolution wave-resolving simulations confirms the effectiveness of this approach. By improving the representation of gravity wave-induced tracer transport, this research advances the accuracy of climate simulations, particularly in their depiction of microphysics and radiative processes.

**KEYWORDS**

gravity waves, tracer transport, parameterization, Stokes drift

## 1 | INTRODUCTION

Accurately simulating the three-dimensional distribution of tracers is crucial for climate modeling, as these tracers have significant radiative effects on Earth's climate. In the zonal mean, large-scale tracer transport—such as that of ozone and water vapor—is primarily governed by thermally and wave-driven global circulations, including the Brewer-Dobson circulation (Butchart, 2014; Brewer, 1949; Dobson, 1956). Small-scale processes, such as gravity waves and turbulence, indirectly influence tracer distributions by driving and modifying these circulations. However, they can also directly affect tracer transport and mixing. Since climate models do not resolve these small-scale processes, their effects must be represented through parameterization.

Previous studies have shown that gravity waves can significantly impact tracer transport (Xu et al., 2002; Walterscheid and Schubert, 1989; Liu and Gardner, 2004). Some parameterization models account for certain aspects of this influence, such as gravity-wave induced vertical mixing of tracers (Gardner et al., 2019). However, a systematic analysis of the governing equations is still lacking, leaving the full nature of gravity wave-induced tracer fluxes uncharacterized. A more refined parameterization is needed to capture these effects comprehensively.

This study aims to address this gap by systematically deriving the key terms that govern how small-scale gravity waves influence large-scale tracer transport. Furthermore, it develops a framework for incorporating these effects into gravity wave parameterization models. To achieve this, we employ a multiple-scale analysis to separate and analyze the interactions between large-scale tracer transport and small-scale gravity waves, identifying the dominant contributions.

Improving the representation of gravity-wave induced tracer transport can enhance climate model accuracy. The framework developed in this study allows for high-accuracy tracer modeling in the presence of gravity waves without explicitly resolving them, significantly improving computational efficiency. Additionally, this research provides a foundation for quantifying the role of non-breaking gravity waves in tracer transport.

This paper is structured as follows. Section 2 derives the inertial and mid-frequency gravity wave-induced tracer transport using a multiple-scale analysis of the governing equations. Using a WKB ansatz, we obtain expressions for wave-induced tracer fluxes in terms of wave amplitudes. We then show how these fluxes can be computed from the phase-space wave action density, a quantity used in gravity wave ray tracing models. The most important equations are summarized in Section 3. Section 4.1 describes the extension of the parameterization model MS-GWaM (see e.g. Bölöni et al., 2016; Wei et al., 2019; Jochum et al., 2025) to include these fluxes and its coupling to an idealized flow solver. We validate the model by comparing its results to wave-resolving reference simulations. Finally, we summarize and conclude our results in Section 5.

## 2 | THEORY OF GRAVITY WAVE-INDUCED TRACER TRANSPORT

This section provides the theoretical basis for understanding the impact of non-breaking, small-scale gravity waves on large-scale tracer transport through gravity wave tracer fluxes. We begin by presenting the governing equations and characteristic scales of gravity waves, then derive expressions for the flux convergences they induce. Using the WKB ansatz, we reformulate these flux convergences in terms of the phase-space wave action density, which serves as the basis for their parameterization.

## 2.1 | Multiple-scale analysis of the governing equations

In this section, we first present the governing equations, including the tracer advection equations. Using the characteristic scales of small-scale gravity waves, we non-dimensionalize these equations and separate terms by order of magnitude in a scale-separation parameter. This approach allows us to identify the terms that describe the impact of gravity waves on large-scale tracer transport.

The advection of a unit-less passive tracer mixing ratio  $\psi$  is given by

$$D_t \psi = 0. \quad (1)$$

The material derivative is defined as  $D_t = \partial_t + \mathbf{v} \cdot \nabla$ , where  $\mathbf{v} = (u, v, w)^T$  with  $u$ ,  $v$ , and  $w$  representing the wind components in the  $x$ -,  $y$ -, and  $z$ -directions, respectively. The wind velocity  $\mathbf{v}$ , potential temperature  $\theta$ , and Exner pressure  $\pi$  are governed by the equations of motion for a dry, inviscid atmosphere

$$D_t \mathbf{u} + f \mathbf{e}_z \times \mathbf{u} = -c_p \theta \nabla_h \pi, \quad (2)$$

$$D_t w = -c_p \theta \partial_z \pi - g, \quad (3)$$

$$D_t \theta = 0, \quad (4)$$

$$D_t \pi + \frac{R}{c_V} \pi \nabla \cdot \mathbf{v} = 0. \quad (5)$$

Here,  $\mathbf{u}$  represents the horizontal wind components,  $c_p$  and  $c_V = c_p - R$  are the specific heat capacities at constant pressure and volume, respectively,  $R$  is the ideal gas constant of dry air,  $g$  is the gravitational acceleration, and  $f$  is the constant Coriolis frequency.

To facilitate the multiple-scale analysis of Equations (1) to (5), we first non-dimensionalize these equations. Following an approach equivalent to Achatz et al. (2017), we define the necessary scales by assuming a hydrostatic reference atmosphere with potential temperature, density, and Exner pressure profiles  $\bar{\theta}(z)$ ,  $\bar{\rho}(z)$ , and  $\bar{\pi}(z)$ , respectively. The Brunt-Väisälä frequency is given by  $N = \sqrt{(g/\bar{\theta}) d_z \bar{\theta}}$ . Depending on the atmospheric stratification, the ratio between the Coriolis frequency and the Brunt-Väisälä frequency is given by  $f/N = O[e^{(5-\delta)/2}]$ , where  $\delta = 0$  or  $\delta = 1$  for a moderately strong or weakly stratified atmosphere, respectively. For  $\delta = 1$ , the weak stratification represents conditions in the troposphere and mesosphere, whereas  $\delta = 0$  corresponds to the strong stability of the stratosphere. Furthermore,  $\varepsilon$  is a small scaling parameter. Using the resulting length, time, and velocity scales summarized in Table 1, we non-dimensionalize Equations (1) to (5), yielding

$$D_t \psi = 0, \quad (6)$$

$$\varepsilon^{2+\delta} (D_t \mathbf{u} + f_0 \mathbf{e}_z \times \mathbf{u}) = -c_p \theta \nabla_h \pi, \quad (7)$$

$$\varepsilon^7 D_t w = -c_p \theta \partial_z \pi - 1, \quad (8)$$

$$D_t \theta = 0, \quad (9)$$

$$D_t \pi + \frac{R}{c_V} \pi \nabla \cdot \mathbf{v} = 0, \quad (10)$$

where  $f_0 = 1$  serves as a non-dimensional placeholder for the Coriolis parameter.

As solutions to Equations (6) to (10), we consider a superposition of expansions in terms of the scale-separation parameter for the reference atmosphere, the large-scale flow, and  $A$  waves described by the WKB ansatz. The vari-

**TABLE 1** Summary of all scaling parameters, with  $\delta = 0$  and 1 for a strongly and weakly stratified atmosphere, respectively, a scaling parameter  $\varepsilon = O(1/10)$ , and a typical atmosphere temperature  $T_{00}$ . Parameters in accordance to Achatz et al. (2023).

| Name                               | Symbol         | Scale size  |
|------------------------------------|----------------|---|
| Horizontal scale                   | $\tilde{L}$    | $\varepsilon^{(2+\delta)/2} \sqrt{RT_{00}}/f$                     |
| Vertical scale                     | $\tilde{H}$    | $\varepsilon^{7/2} \sqrt{RT_{00}}/f$                              |
| Time scale                         | $\tilde{T}$    | $1/f$   |
| Horizontal velocity                | $\tilde{U}$    | $\tilde{L}/\tilde{T} = \varepsilon^{(2+\delta)/2} \sqrt{RT_{00}}$ |
| Vertical velocity                  | $\tilde{W}$    | $\tilde{H}/\tilde{T} = \varepsilon^{7/2} \sqrt{RT_{00}}$          |
| Characteristic tracer mixing ratio | $\tilde{\Psi}$ | 1   |

ables thus take the form

$$\psi(\mathbf{x}, t) = \sum_{m=0}^{\infty} \varepsilon^m \langle \Psi \rangle^{(m)}(\mathbf{X}, T) + \Re \sum_{\alpha=1}^A \sum_{\beta=1}^{\infty} \sum_{m=0}^{\infty} \varepsilon^m \hat{\Psi}_{\alpha\beta}^{(m)}(\mathbf{X}, T) e^{i\beta\phi_{\alpha}(\mathbf{X}, T)/\varepsilon}, \quad (11)$$

$$\mathbf{v}(\mathbf{x}, t) = \sum_{m=0}^{\infty} \varepsilon^m \langle \mathbf{V} \rangle^{(m)}(\mathbf{X}, T) + \varepsilon^{\gamma} \Re \sum_{\alpha=1}^A \sum_{\beta=1}^{\infty} \sum_{m=0}^{\infty} \varepsilon^m \hat{\mathbf{V}}_{\alpha\beta}^{(m)}(\mathbf{X}, T) e^{i\beta\phi_{\alpha}(\mathbf{X}, T)/\varepsilon}, \quad (12)$$

$$\begin{aligned} \theta(\mathbf{x}, t) &= \sum_{m=0}^{\delta} \varepsilon^m \bar{\Theta}^{(m)}(Z) + \varepsilon^{\delta+1} \sum_{m=0}^{\infty} \varepsilon^m \langle \Theta \rangle^{(m)}(\mathbf{X}, T) \\ &+ \varepsilon^{\gamma+\delta+1} \Re \sum_{\alpha=1}^A \sum_{\beta=1}^{\infty} \sum_{m=0}^{\infty} \varepsilon^m \hat{\Theta}_{\alpha\beta}^{(m)}(\mathbf{X}, T) e^{i\beta\phi_{\alpha}(\mathbf{X}, T)/\varepsilon}, \end{aligned} \quad (13)$$

$$\begin{aligned} \pi(\mathbf{x}, t) &= \sum_{m=0}^{\delta} \varepsilon^m \bar{\Pi}^{(m)}(Z) + \varepsilon^{\delta+1} \sum_{m=0}^{\infty} \varepsilon^m \langle \Pi \rangle^{(m)}(\mathbf{X}, T) \\ &+ \varepsilon^{\gamma+\delta+2} \Re \sum_{\alpha=1}^A \sum_{\beta=1}^{\infty} \sum_{m=0}^{\infty} \varepsilon^m \hat{\Pi}_{\alpha\beta}^{(m)}(\mathbf{X}, T) e^{i\beta\phi_{\alpha}(\mathbf{X}, T)/\varepsilon}. \end{aligned} \quad (14)$$

The Exner pressure and potential temperature profiles of the reference atmosphere are denoted by  $\bar{\Pi}^{(m)}$  and  $\bar{\Theta}^{(m)}$ , respectively, while large-scale variables are represented using angle brackets. The remaining variables, proportional to  $e^{i\beta\phi_{\alpha}/\varepsilon}$ , correspond to wave contributions, where  $\beta = 1$  represents a fundamental wave and  $\beta = 2, 3, \dots$  denote its second, third, and higher harmonics. To emphasize the slow variation of the large-scale flow, wave amplitudes, and local wavenumbers  $\beta \mathbf{k}_{\alpha} = \beta \nabla \phi_{\alpha} / \varepsilon = \beta \nabla_{\mathbf{X}} \phi_{\alpha}$  and frequencies  $\beta \omega_{\alpha} = -\beta \partial_t \phi_{\alpha} / \varepsilon = -\beta \partial_T \phi_{\alpha}$ , we introduce the slow variables  $(\mathbf{X}, T) = \varepsilon(\mathbf{x}, t)$ . Additionally, the wave components of wind, potential temperature, and Exner pressure include a factor  $\varepsilon^{\gamma}$  to account for different wave amplitude cases. We distinguish three regimes: large-amplitude waves ( $\gamma = 0$ ), weakly nonlinear waves ( $\gamma = 1$ ), and quasi-linear waves ( $\gamma = 2$ ). Each regime requires a slightly different treatment. For  $\gamma = 0$ , we assume monochromatic waves with  $A = 1$ . In the weakly nonlinear case ( $\gamma = 1$ ), we allow for a spectrum of gravity waves ( $A \geq 1$ ) but neglect wave-wave interactions affecting the gravity wave itself. Only the quasi-linear case does not require these previous assumptions. We impose no amplitude assumptions on the tracer field, allowing us to determine its magnitude from the governing equations.

Before proceeding with the multiple-scale analysis of the tracer advection equation, we briefly outline how we

handle the  $\varepsilon$ -expansion of the large-scale and background atmosphere variables and introduce a compact notation, which will be used throughout Section 2. Equations (11) to (14) present the full expansion of the large-scale and reference atmosphere variables in  $\varepsilon$ . In a rigorous asymptotic expansion of Equations (6) to (10), we would account for the different orders of magnitude in  $\varepsilon$  for these variables, as done in Achatz et al. (2023). However, since the equations in this paper are designed for numerical implementation, we retain the full expansion rather than isolating specific orders in  $\varepsilon$ . This approach is necessary, because, in numerical models, the large-scale variables represent the full resolved flow without any expansion in  $\varepsilon$ . To streamline notation, we introduce a compact representation for the large-scale variables, exemplified here for the large-scale tracer

$$\sum_{m=0}^{\infty} \varepsilon^m \langle \Psi \rangle^{(m)} \equiv \langle \Psi \rangle, \quad (15)$$

with equivalent notation for the large-scale winds, Exner pressure, and potential temperature. Additionally, the Exner pressure and potential temperature of the reference atmosphere are denoted by

$$\sum_{m=0}^{\delta} \varepsilon^m \bar{\Pi}^{(m)} \equiv \bar{\Pi} \quad \text{and} \quad \sum_{m=0}^{\delta} \varepsilon^m \bar{\Theta}^{(m)} \equiv \bar{\Theta}, \quad (16)$$

respectively.

We now proceed with the multiple-scale analysis of the tracer advection equation, aiming to identify the dominant terms that describe the impact of gravity waves on large-scale tracer transport. By substituting the decompositions from Equations (11) and (12) into Equation (6) and sorting terms by powers of  $\varepsilon$  and the phase factor  $e^{i\beta\phi_\alpha/\varepsilon}$ , we find that the first nonzero tracer wave amplitude,  $\hat{\Psi}_{\alpha\beta}^{(\gamma+1)}$ , is related to the leading-order wind amplitude by

$$i\beta\hat{\omega}_\alpha \hat{\Psi}_{\alpha\beta}^{(\gamma+1)} = \hat{\mathbf{V}}_{\alpha\beta}^{(0)} \cdot \nabla_{\mathbf{X}} \langle \Psi \rangle, \quad (17)$$

where  $\hat{\omega}_\alpha = \omega_\alpha - \mathbf{k}_{h,\alpha} \cdot \langle \mathbf{V} \rangle$  is the intrinsic frequency. The next-to-leading-order tracer amplitudes are given by the relation

$$i\beta\hat{\omega}_\alpha \hat{\Psi}_{\alpha\beta}^{(\gamma+2)} = (\partial_\tau + \langle \mathbf{U} \rangle \cdot \nabla_{\mathbf{X},h}) \hat{\Psi}_{\alpha\beta}^{(\gamma+1)} + \hat{\mathbf{V}}_{\alpha\beta}^{(1)} \cdot \nabla_{\mathbf{X}} \langle \Psi \rangle. \quad (18)$$

These results also account for the factor that the leading-order large-scale vertical wind,  $\langle W \rangle^{(0)} = 0$ , vanishes, as demonstrated in Achatz et al. (2023). To derive the result for  $\gamma = 1$ , we neglect the triad terms in Equation (18) associated with wave-wave interactions. Using the large-scale terms and the relations above, we obtain the following equation for the large-scale tracer mixing ratio

$$\begin{aligned} \varepsilon (\partial_\tau + \langle \mathbf{V} \rangle \cdot \nabla_{\mathbf{X}}) \langle \Psi \rangle = & -\frac{\varepsilon^\gamma}{2} \sum_{\alpha=1}^A \sum_{\beta=1}^{\infty} \sum_{m=0}^{\infty} \sum_{n=\gamma+1}^{\infty} \varepsilon^{(m+n+1)} \Re \left( \hat{\mathbf{V}}_{\alpha\beta}^{(m)} \cdot \nabla_{\mathbf{X}} \hat{\Psi}_{\alpha\beta}^{(n)*} \right) \\ & + \varepsilon^{(m+n)} \Im \left( \hat{\mathbf{V}}_{\alpha\beta}^{(m)} \cdot \beta \mathbf{k}_\alpha \hat{\Psi}_{\alpha\beta}^{(n)*} \right). \end{aligned} \quad (19)$$

Additionally, using the wind amplitude relations derived from the Exner pressure equation (Equation (10))

$$i\beta \mathbf{k}_\alpha \cdot \hat{\mathbf{V}}_{\alpha\beta}^{(0)} = 0, \quad (20)$$

$$i\beta \mathbf{k}_\alpha \cdot \hat{\mathbf{V}}_{\alpha\beta}^{(1)} = -\frac{1}{\bar{P}} \nabla_{\mathbf{X}} \cdot \left( \bar{P} \hat{\mathbf{V}}_{\alpha\beta}^{(0)} \right), \quad (21)$$

$$i\beta \mathbf{k}_\alpha \cdot \hat{\mathbf{V}}_{\alpha\beta}^{(2)} = -\frac{1}{\bar{P}} \nabla_{\mathbf{X}} \cdot \left( \bar{P} \hat{\mathbf{V}}_{\alpha\beta}^{(1)} \right), \quad (22)$$

where  $\bar{P} = \bar{\rho}\bar{\theta}$  is the mass-weighted potential temperature of the reference atmosphere, we find that Equation (22) is strictly valid for  $\delta = 0$ , except for a small correction that we ignore in the following analysis. Consequently, Equation (19) can be rewritten as

$$\varepsilon \left( \partial_t + \langle \mathbf{U} \rangle \cdot \nabla_{\mathbf{X}} \right) \langle \Psi \rangle = Q^{(0)} + Q^{(1)} + O \left[ \varepsilon^{(2\gamma+4)} \right]. \quad (23)$$

The leading-order terms on the right-hand side of Equation (19), summarized in Equation (23) as  $Q^{(0)}$ , are  $O \left( \varepsilon^{(2\gamma+1)} \right)$  smaller than the large-scale advection and can be rewritten as

$$Q^{(0)} \equiv -\frac{\varepsilon^{(2\gamma+2)}}{2\bar{P}} \sum_{\alpha=1}^A \nabla_{\mathbf{X}} \cdot \Re \left( \bar{P} \hat{\mathbf{V}}_{\alpha 1}^{(0)} \hat{\Psi}_{\alpha 1}^{(\gamma+1)*} \right). \quad (24)$$

Here, we use the fact that higher harmonics with  $\beta > 1$  do not contribute, since for those,  $\hat{\mathbf{V}}_{\alpha\beta}^{(0)} = 0$  (Achatz et al., 2023) and, by Equation (17), also  $\hat{\Psi}_{\alpha\beta}^{(\gamma+1)} = 0$ . Similarly, all terms in Equation (19) that are  $O \left( \varepsilon^{(2\gamma+2)} \right)$  smaller than the large-scale advection are grouped into  $Q^{(1)}$  in Equation (23) and can be rewritten as

$$Q^{(1)} \equiv -\frac{\varepsilon^{(2\gamma+3)}}{2\bar{P}} \sum_{\alpha=1}^A \nabla_{\mathbf{X}} \cdot \Re \left[ \bar{P} \left( \hat{\mathbf{V}}_{\alpha 1}^{(0)} \hat{\Psi}_{\alpha 1}^{(\gamma+2)*} + \hat{\mathbf{V}}_{\alpha 1}^{(1)} \hat{\Psi}_{\alpha 1}^{(\gamma+1)*} \right) \right]. \quad (25)$$

With gravity wave parameterization in mind, it is convenient to express the terms in Equations (24) and (25) using variables commonly computed in parameterization models, such as the wave action density and wavenumbers. These formulation will be presented in the following sections.

## 2.2 | Leading-order gravity wave tracer flux convergence

In this section, we describe how to calculate the leading-order gravity wave tracer flux convergence,  $Q^{(0)}$ , in Equation (24) using the wave action density and wavenumbers predicted by a gravity wave model.

We aim to describe  $Q^{(0)}$  in terms of the wave action density,  $\mathcal{A}_\alpha = E_{w,\alpha} / \hat{\omega}_\alpha$ , where  $E_{w,\alpha}$  is the wave energy given by Achatz et al. (2023) as

$$E_{w,\alpha} = \frac{\bar{P}}{2} \left( \frac{|\hat{\mathbf{U}}_{\alpha 1}^{(0)}|^2}{2} + \varepsilon^{5-\delta} \frac{|\hat{\mathbf{W}}_{\alpha 1}^{(0)}|^2}{2} + \frac{1}{N_0^2} \frac{|\hat{\mathbf{B}}_{\alpha 1}^{(0)}|^2}{2} \right) = \frac{\bar{P}}{2} \frac{|\hat{\mathbf{B}}_{\alpha 1}^{(0)}|^2}{2N_0^2} \frac{N_0^2 k_{h,\alpha}^2 + f_0^2 m_\alpha^2}{N_0^2 k_{h,\alpha}^2}, \quad (26)$$

$\hat{\mathbf{B}}_{\alpha 1}^{(0)} = \hat{\omega}_{\alpha 1}^{(0)} / \bar{\Theta}$  is the leading-order buoyancy amplitude, and the horizontal wavenumber  $k_{h,\alpha}$  is defined as  $k_{h,\alpha} =$

$\sqrt{k_\alpha^2 + l_\alpha^2}$ . The dispersion relation for internal gravity waves is given by

$$\hat{\omega}_\alpha^2 = \frac{N_0^2 k_{h,\alpha}^2 + f_0^2 m_\alpha^2}{\varepsilon^{5-\delta} k_{h,\alpha}^2 + m_\alpha^2}. \quad (27)$$

Therefore, we must express the leading-order tracer and wind amplitudes,  $\hat{\Psi}_{\alpha 1}^{(\gamma+1)}$  and  $\hat{\mathbf{V}}_{\alpha 1}^{(0)}$ , respectively, in terms of the buoyancy amplitude  $\hat{B}_{\alpha 1}^{(0)}$ . The tracer amplitude is coupled to the wind amplitude via Equation (17). The wind amplitude, in turn, is coupled to the buoyancy amplitude through the polarization relations (Achatz et al., 2017, 2023)

$$\hat{\mathbf{U}}_{\alpha 1}^{(0)} = \frac{i}{m_\alpha N_0^2} \frac{\varepsilon^{5-\delta} \hat{\omega}_\alpha^2 - N_0^2}{\hat{\omega}_\alpha^2 - f_0^2} (\mathbf{k}_{h,\alpha} \hat{\omega}_\alpha - i f_0 \mathbf{e}_z \times \mathbf{k}_{h,\alpha}) \hat{B}_{\alpha 1}^{(0)}, \quad (28)$$

$$\hat{W}_{\alpha 1}^{(0)} = \frac{i \hat{\omega}_\alpha}{N_0^2} \hat{B}_{\alpha 1}^{(0)}, \quad (29)$$

$$\frac{c_p}{R} \bar{\Theta}_{\alpha 1}^{(0)} = \frac{i}{m_\alpha} \frac{\varepsilon^{5-\delta} \hat{\omega}_\alpha^2 - N_0^2}{N_0^2} \hat{B}_{\alpha 1}^{(0)}. \quad (30)$$

As it is needed later on, we have also included the polarization relation for the Exner pressure. These relations are derived from the matrix equation

$$M_{\alpha 1} \mathbf{Z}_{\alpha 1}^{(0)} = 0, \quad (31)$$

where the matrix  $M_{\alpha 1}$  is given by

$$M_{\alpha 1} = M(\mathbf{k}_\alpha, \hat{\omega}_\alpha) = \begin{bmatrix} -i \hat{\omega}_\alpha & -f_0 & 0 & 0 & i k_\alpha \\ f_0 & -i \hat{\omega}_\alpha & 0 & 0 & i l_\alpha \\ 0 & 0 & -i \hat{\omega}_\alpha \varepsilon^{5-\delta} & -N_0 & i m_\alpha \\ 0 & 0 & N_0 & -i \hat{\omega}_\alpha & 0 \\ i k_\alpha & i l_\alpha & i m_\alpha & 0 & 0 \end{bmatrix}, \quad (32)$$

the components of the wave numbers are denoted by  $\mathbf{k}_\alpha = (k_\alpha, l_\alpha, m_\alpha)^\top$ , and the vector  $\mathbf{Z}_{\alpha 1}^{(0)}$  contains the wave amplitudes

$$\mathbf{Z}_{\alpha 1}^{(0)} = \left( \hat{U}_{\alpha 1}^{(0)}, \hat{V}_{\alpha 1}^{(0)}, \hat{W}_{\alpha 1}^{(0)}, \hat{B}_{\alpha 1}^{(0)} / N_0, \frac{c_p}{R} \bar{\Theta}_{\alpha 1}^{(0)} \right)^\top. \quad (33)$$

The non-dimensional Brunt-Väisälä frequency is defined as  $N_0^2 = d_Z \bar{\Theta}^{(\delta)} / \bar{\Theta}$ .

By inserting Equations (17) and (26) to (29) into Equation (24), we obtain an expression for  $Q^{(0)}$  in terms of the wave action density:

$$Q^{(0)} = -\frac{\varepsilon^{(2\gamma+1)}}{\bar{\rho}} \sum_{\alpha=1}^A \nabla_{\mathbf{X}} \cdot \left( \frac{f_0}{\hat{\omega}_\alpha} \frac{m_\alpha}{\varepsilon^{5-\delta} k_{h,\alpha}^2 + m_\alpha^2} \mathcal{A}_\alpha \mathbf{k}_\alpha \times \nabla_{\mathbf{X}} \langle \Psi \rangle \right). \quad (34)$$

## 2.3 | Next-order gravity wave tracer flux convergence

Similar to the previous section, we now describe how the next-order flux convergence,  $Q^{(1)}$ , can be determined from the wave action density.

The next-order flux convergence,  $Q^{(1)}$ , is given in Equation (25). Since  $\mathcal{A}_\alpha \propto |\hat{\beta}_{\alpha 1}^{(0)}|^2$ , both the leading-order and next-order tracer and wind amplitudes must be expressed in terms of the buoyancy amplitude. As described in the previous section, the leading-order amplitudes are coupled to  $\hat{\beta}_{\alpha 1}^{(0)}$  via Equations (17), (28) and (29). The next-order tracer amplitudes can be obtained from the next-order wind amplitudes and the leading-order tracer amplitudes, as shown in Equation (18). Therefore, the remaining task is to determine  $\hat{\mathbf{V}}_{\alpha 1}^{(1)}$  in terms of  $\hat{\beta}_{\alpha 1}^{(0)}$ . Similar to the leading-order basic wave amplitudes, the next-order wind, buoyancy and Exner pressure amplitudes  $\hat{\mathbf{V}}_{\alpha 1}^{(1)}$ ,  $\hat{\beta}_{\alpha 1}^{(1)} = \hat{\Theta}_{\alpha 1}^{(1)}/\bar{\Theta}$ , and  $\hat{\Pi}_{\alpha 1}^{(1)}$ , respectively, satisfy a matrix equation

$$M_{\alpha 1} \mathbf{Z}_{\alpha 1}^{(1)} = \mathbf{R}_{\alpha 1}^{(1)}, \quad (35)$$

where  $M_{\alpha 1}$  given in Equation (32),

$$\mathbf{Z}_{\alpha 1}^{(1)} = \left( \hat{U}_{\alpha 1}^{(1)}, \hat{V}_{\alpha 1}^{(1)}, \hat{W}_{\alpha 1}^{(1)}, \hat{\beta}_{\alpha 1}^{(1)}/N_0, \frac{c_p}{R} \bar{\Theta} \hat{\Pi}_{\alpha 1}^{(1)} \right)^T, \quad (36)$$

and

$$\mathbf{R}_{\alpha 1}^{(1)} = (R_{u,\alpha 1}, R_{v,\alpha 1}, R_{w,\alpha 1}, R_{b,\alpha 1}/N_0, R_{\pi,\alpha 1})^T. \quad (37)$$

The components of  $\mathbf{R}_{\alpha 1}^{(1)}$  are

$$\mathbf{R}_{u,\alpha 1}^{(1)} = - \left( \partial_T + \langle \mathbf{U} \rangle \cdot \nabla_{X,h} \right) \hat{U}_{\alpha 1}^{(0)} - \left( \hat{V}_{\alpha 1}^{(0)} \cdot \nabla_X \right) \langle \mathbf{U} \rangle - \frac{c_p}{R} \left[ \bar{\Theta} \nabla_{X,h} \hat{\Pi}_{\alpha 1}^{(0)} + \varepsilon^\delta \left( i \mathbf{k}_{h,\alpha} \langle \Theta \rangle \hat{\Pi}_{\alpha 1}^{(0)} + \hat{\Theta}_{\alpha 1}^{(0)} \nabla_{X,h} \langle \Pi \rangle \right) \right], \quad (38)$$

$$\mathbf{R}_{w,\alpha 1}^{(1)} = - \varepsilon^{5-\delta} \left( \partial_T + \langle \mathbf{U} \rangle \cdot \nabla_{X,h} \right) \hat{W}_{\alpha 1}^{(0)} - \frac{c_p}{R} \left[ \bar{\Theta} \partial_Z \hat{\Pi}_{\alpha 1}^{(0)} + \varepsilon^\delta \left( i m_\alpha \langle \Theta \rangle \hat{\Pi}_{\alpha 1}^{(0)} + \hat{\Theta}_{\alpha 1}^{(0)} \partial_Z \langle \Pi \rangle \right) \right], \quad (39)$$

$$\mathbf{R}_{b,\alpha 1}^{(1)} = - \left( \partial_T + \langle \mathbf{U} \rangle \cdot \nabla_{X,h} \right) \hat{\beta}_{\alpha 1}^{(0)} - \frac{\hat{V}_{\alpha 1}^{(0)}}{\bar{\Theta}} \cdot \nabla_X \langle \Theta \rangle, \quad (40)$$

$$\mathbf{R}_{\pi,\alpha 1}^{(1)} = - \frac{1}{\bar{P}} \nabla_X \cdot \left( \bar{P} \hat{\mathbf{V}}_{\alpha 1}^{(0)} \right), \quad (41)$$

with  $\mathbf{R}_{u,\alpha 1}^{(1)} = \left( R_{u,\alpha 1}^{(1)}, R_{v,\alpha 1}^{(1)} \right)^T$ . These right-hand sides follow Achatz et al. (2017). However, in contrast to that work, we have included higher-order terms from the case  $\delta = 1$  to facilitate a unified treatment of the two stratification cases. Likewise, we retain the full expansion of the advection large-scale winds. Using the polarization relations from Equations (28) to (30), all right-hand sides can be determined from the spatial and temporal dependence of the wavenumber and leading-order buoyancy amplitude  $\hat{\beta}_{\alpha 1}^{(0)}$ . Once these terms are known, the next-order wave amplitudes  $\mathbf{Z}_{\alpha 1}^{(1)}$  can be obtained by solving Equation (35). It is important to note that the next-order amplitude vector  $\mathbf{Z}_{\alpha 1}^{(1)}$  does not belong to the null space of  $M_{\alpha 1}$ , as the latter is assumed to only contribute to the basic-wave amplitudes  $\mathbf{Z}_{\alpha 1}^{(0)}$ .

The leading-order buoyancy amplitude, required for all subsequent calculation, can be decomposed into its absolute magnitude and phase factor

$$\hat{\beta}_{\alpha 1}^{(0)} = \left| \hat{\beta}_{\alpha 1}^{(0)} \right| e^{i\Lambda_\alpha}, \quad (42)$$



where  $\Lambda_\alpha$  represents the large-scale wave amplitude. The absolute magnitude can be obtained from the wave energy  $E_{w,\alpha}$  via Equation (26). While  $E_{w,\alpha}$  is directly available from the gravity wave model, the large-scale phase must be predicted from the prognostic equation

$$\begin{aligned} (\partial_T + \mathbf{c}_{g,\alpha} \cdot \nabla_{\mathbf{X}}) \Lambda_\alpha = & - \frac{f_0 m_\alpha}{2 |\mathbf{k}_\alpha|^2 \hat{\omega}_\alpha} (\mathbf{k}_\alpha \times \nabla_{\mathbf{X}}) \langle \mathbf{U} \rangle \\ & + \frac{N_0^2}{2 (N_0^2 - \varepsilon^{5-\delta} f_0^2) m_\alpha} \left[ \varepsilon^\delta \frac{c_p}{R} \bar{\Theta} (\hat{\mathbf{c}}_{g,\alpha} \cdot \nabla_{\mathbf{X}}) \langle \Pi \rangle + \frac{1}{N_0^2} \frac{1}{\bar{\Theta}} (\hat{\mathbf{c}}_{g,\alpha} \cdot \nabla_{\mathbf{X}}) \langle \Theta \rangle \right] \\ & - \frac{f_0 m_\alpha^2}{|\mathbf{k}_\alpha|^4 \hat{\omega}_\alpha} \left[ (k_\alpha \partial_Y - l_\alpha \partial_X) \hat{\omega}_\alpha + l_\alpha (\partial_T + \langle \mathbf{U} \rangle \cdot \nabla_{\mathbf{X},h}) k_\alpha - k_\alpha (\partial_T + \langle \mathbf{U} \rangle \cdot \nabla_{\mathbf{X},h}) l_\alpha \right], \end{aligned} \quad (43)$$

where  $\mathbf{c}_{g,\alpha} = \nabla_{\mathbf{k}} \omega_\alpha$  is the group velocity and  $\hat{\mathbf{c}}_{g,\alpha} = \nabla_{\mathbf{k}} \hat{\omega}_\alpha$  is the intrinsic group velocity. We derive the prognostic equation by taking the imaginary part of the solvability condition, as outlined in Achatz et al. (2010):

$$0 = \mathbf{Z}_{\alpha 1}^{(0)\dagger} \mathbf{R}_{\alpha 1}^{(1)}. \quad (44)$$

In summary,  $\hat{\mathbf{B}}_{\alpha 1}^{(0)}$  in Equation (42) can be calculated using Equations (26) and (43). The leading-order tracer and wind amplitudes can then be determined from Equation (17) and Equations (28) and (29), respectively. Next, by solving Equation (35) for  $\mathbf{Z}_{\alpha 1}^{(1)}$  and using Equation (18), the next-order tracer and wind amplitudes can be computed. Finally, the resulting  $\hat{\Psi}_{\alpha 1}^{(\gamma+1)}$ , can be substituted into Equation (25) to obtain  $Q^{(1)}$ .

### 3 | SUMMARY OF EQUATIONS IN DIMENSIONAL FORM

Finally, we summarize the most important equations in dimensional form. To achieve this, we make the following substitutions:

$$\hat{\omega} \rightarrow \hat{\omega} \tilde{T} = \hat{\omega} / f \quad (45)$$

$$(X, Y, Z) \rightarrow \varepsilon \left[ (x, y) / \tilde{L}, z / \tilde{H} \right] \quad (46)$$

$$T \rightarrow \varepsilon t / \tilde{T} \quad (47)$$

$$(k, l, m) \rightarrow \left[ \tilde{L}(k, l), \tilde{H}m \right] \quad (48)$$

$$f_0 \rightarrow f / f \quad (49)$$

$$\bar{\Theta} \rightarrow \bar{\theta} / T_{00} \quad (50)$$

$$[\langle \mathbf{U} \rangle, \langle \mathbf{W} \rangle, \langle \Psi \rangle, \langle \Theta \rangle, \langle \Pi \rangle] \rightarrow \left[ \frac{\langle \mathbf{u} \rangle}{\tilde{U}}, \frac{\langle \mathbf{w} \rangle}{\varepsilon \tilde{W}}, \frac{\langle \psi \rangle}{\tilde{\Psi}}, \frac{\langle \theta \rangle}{\varepsilon^{\delta+1} T_{00}}, \frac{\langle \pi \rangle}{\varepsilon^{\delta+1}} \right]. \quad (51)$$

With the dispersion relation

$$\hat{\omega}_\alpha^2 = \frac{N^2 k_{h,\alpha}^2 + f^2 m_\alpha^2}{k_{h,\alpha}^2 + m_\alpha^2}, \quad (52)$$

where  $N^2 = (g/\bar{\theta})d_z\bar{\theta}$ , and the substitution for the leading-order wave amplitudes

$$\left( \hat{\mathbf{U}}_{\alpha 1}^{(0)}, \hat{W}_{\alpha 1}^{(0)}, \hat{B}_{\alpha 1}^{(0)}, \hat{\Pi}_{\alpha 1}^{(0)}, \hat{\Psi}_{\alpha 1}^{(\gamma+1)} \right) \rightarrow \left( \frac{\mathbf{u}'_{\alpha}}{U}, \frac{w'_{\alpha}}{W}, \frac{\theta'_{\alpha}}{\varepsilon^{\delta+1}\bar{\theta}}, \frac{\pi'_{\alpha}}{\varepsilon^{\delta+2}}, \frac{\psi'_{\alpha}}{\varepsilon^{\gamma}} \right) \frac{1}{\varepsilon^{\gamma}}, \quad (53)$$

we obtain the polarization relations

$$\mathbf{u}'_{\alpha} = \frac{i}{m_{\alpha}N^2} \frac{\hat{\omega}_{\alpha}^2 - N^2}{\hat{\omega}_{\alpha}^2 - f^2} (\mathbf{k}_{h,\alpha}\hat{\omega}_{\alpha} - if\mathbf{e}_z \times \mathbf{k}_{h,\alpha}) b'_{\alpha}, \quad (54)$$

$$w'_{\alpha} = \frac{i\hat{\omega}_{\alpha}}{N^2} b'_{\alpha}, \quad (55)$$

$$c_p\bar{\theta}\pi'_{\alpha} = \frac{i}{m_{\alpha}} \frac{\hat{\omega}_{\alpha}^2 - N^2}{N^2} b'_{\alpha}. \quad (56)$$

The leading-order tracer amplitude is given by

$$\psi'_{\alpha} = -\frac{i}{\hat{\omega}_{\alpha}} \mathbf{v}'_{\alpha} \cdot \nabla \langle \psi \rangle. \quad (57)$$

The re-dimensionalized matrix equation (35) is expressed as

$$\underbrace{\begin{bmatrix} -i\hat{\omega}_{\alpha} & -f & 0 & 0 & ik_{\alpha} \\ f & -i\hat{\omega}_{\alpha} & 0 & 0 & il_{\alpha} \\ 0 & 0 & -i\hat{\omega}_{\alpha} & -N & im_{\alpha} \\ 0 & 0 & N & -i\hat{\omega}_{\alpha} & 0 \\ ik_{\alpha} & il_{\alpha} & im_{\alpha} & 0 & 0 \end{bmatrix}}_{M_{\alpha}} \underbrace{\begin{bmatrix} u''_{\alpha} \\ v''_{\alpha} \\ w''_{\alpha} \\ b''_{\alpha}/N \\ c_p\bar{\theta}\pi''_{\alpha} \end{bmatrix}}_{\mathbf{Z}''_{\alpha}} = \underbrace{\begin{bmatrix} R_{u,\alpha} \\ R_{v,\alpha} \\ R_{w,\alpha} \\ R_{b,\alpha}/N \\ R_{\pi,\alpha} \end{bmatrix}}_{\mathbf{R}_{\alpha}}, \quad (58)$$

where the next-order wave amplitudes are obtained through the substitution

$$\left( \hat{\mathbf{U}}_{\alpha 1}^{(1)}, \hat{W}_{\alpha 1}^{(1)}, \hat{B}_{\alpha 1}^{(1)}, \hat{\Pi}_{\alpha 1}^{(1)}, \hat{\Psi}_{\alpha 1}^{(\gamma+2)} \right) \rightarrow \left( \frac{\mathbf{u}''_{\alpha}}{U}, \frac{w''_{\alpha}}{W}, \frac{\theta''_{\alpha}}{\varepsilon^{\delta+1}\bar{\theta}}, \frac{\pi''_{\alpha}}{\varepsilon^{\delta+2}}, \frac{\psi''_{\alpha}}{\varepsilon^{\gamma}} \right) \frac{1}{\varepsilon^{\gamma+1}}, \quad (59)$$

and the components of  $\mathbf{R}_{\alpha}$  are

$$\mathbf{R}_{u,\alpha} = -(\partial_t + \langle \mathbf{u} \rangle \cdot \nabla_h) \mathbf{u}'_{\alpha} - \mathbf{v}'_{\alpha} \cdot \nabla \langle \mathbf{u} \rangle - c_p \left[ \bar{\theta} \nabla_h \pi'_{\alpha} + i\mathbf{k}_{h,\alpha} \langle \theta \rangle \pi'_{\alpha} + \theta'_{\alpha} \nabla_h \langle \pi \rangle \right], \quad (60)$$

$$R_{w,\alpha} = -(\partial_t + \langle \mathbf{u} \rangle \cdot \nabla_h) w'_{\alpha} - c_p \left[ \bar{\theta} \partial_z \pi'_{\alpha} + im_{\alpha} \langle \theta \rangle \pi'_{\alpha} + \theta'_{\alpha} \partial_z \langle \pi \rangle \right], \quad (61)$$

$$R_{b,\alpha} = -(\partial_t + \langle \mathbf{u} \rangle \cdot \nabla_h) b'_{\alpha} - \frac{\mathbf{v}'_{\alpha}}{\bar{\theta}} \cdot \nabla \langle \theta \rangle, \quad (62)$$

$$R_{\pi,\alpha} = -\frac{1}{\bar{\rho}\bar{\theta}} \nabla \cdot (\bar{\rho}\bar{\theta}\mathbf{v}'_{\alpha}). \quad (63)$$

The next-order tracer amplitude is given by

$$i\hat{\omega}_{\alpha}\psi''_{\alpha} = -(\partial_t + \langle \mathbf{u} \rangle \cdot \nabla_h) \psi'_{\alpha} + \mathbf{v}'_{\alpha} \cdot \nabla \langle \psi \rangle. \quad (64)$$

Re-dimensionalized, the gravity wave-induced tracer Stokes drift  $Q^{(0)}$  is

$$Q^{(0)} = -\frac{1}{\bar{\rho}} \nabla \cdot \sum_{\alpha=1}^A \frac{f}{\hat{\omega}_\alpha} \frac{m_\alpha}{k_{h,\alpha}^2 + m_\alpha^2} \mathcal{A}_\alpha \mathbf{k}_\alpha \times \nabla \langle \psi \rangle, \quad (65)$$

while the next-order gravity wave-impact

$$Q^{(1)} = -\frac{1}{2\bar{\rho}\bar{\theta}} \sum_{\alpha=1}^A \nabla \cdot \Re \left[ \bar{\rho}\bar{\theta} (\mathbf{v}'_\alpha \psi''_{\alpha*} + \mathbf{v}'_{\alpha*} \psi''_\alpha) \right] \quad (66)$$

is determined through a sequential process:

1. Solving for the leading-order buoyancy amplitude  $b'_{\alpha 1} = |b'_{\alpha 1}| e^{i\Lambda_\alpha}$  from the wave energy equation

$$E_{w,\alpha} = \frac{\bar{\rho}}{2} \left( \frac{|\mathbf{v}'_\alpha|^2}{2} + \frac{|b'_{\alpha 1}|^2}{2N^2} \right) = \bar{\rho} \frac{|b'_{\alpha 1}|^2}{2N^2} \frac{N^2 k_{h,\alpha}^2 + f^2 m_\alpha^2}{N^2 k_{h,\alpha}^2}. \quad (67)$$

2. Integrating the prognostic equation for  $\Lambda_\alpha$  to obtain its large-scale phase:

$$\begin{aligned} (\partial_t + \mathbf{c}_{g,\alpha} \cdot \nabla) \Lambda_\alpha &= -\frac{f m_\alpha}{2 |\mathbf{k}_\alpha|^2 \hat{\omega}_\alpha} (\mathbf{k}_\alpha \times \nabla) \langle \mathbf{u} \rangle \\ &+ \frac{N^2}{2(N^2 - f^2) m_\alpha} \left[ c_{p\bar{\theta}} (\hat{\mathbf{c}}_{g,\alpha} \cdot \nabla) \langle \pi \rangle + \frac{1}{\bar{\theta} N^2} (\hat{\mathbf{c}}_{g,\alpha} \cdot \nabla) \langle \theta \rangle \right] \\ &- \frac{f m_\alpha^2}{|\mathbf{k}_\alpha|^4 \hat{\omega}_\alpha} \left[ (k_\alpha \partial_y + l_\alpha \partial_x) \hat{\omega}_\alpha + l_\alpha (\partial_t + \langle \mathbf{u} \rangle \cdot \nabla_h) k_\alpha - k_\alpha (\partial_t + \langle \mathbf{u} \rangle \cdot \nabla_h) l_\alpha \right]. \end{aligned} \quad (68)$$

3. Using the polarization relations (Equations (54) to (56)) to compute the leading-order wind and pressure amplitudes.
4. Determining the right-hand sides (Equations (60) to (63) of Equation (58)) of Equation (58) based on the leading-order wave amplitudes.
5. Solving Equation (58) for the next-order wind amplitudes.
6. Computing the leading-order tracer amplitude from Equation (57) and the next-order tracer amplitude from Equation (64).
7. Finally, substituting these values, along with the leading-order and next-order wind amplitudes, into Equation (66) to obtain  $Q^{(1)}$ .

Since  $\det(M_\alpha) = 0$  (leading to the dispersion relation  $\hat{\omega}_\alpha$  in Equation (52)), the matrix  $M_\alpha$  is not invertible. However, by computing the pseudo-inverse  $M_\alpha^{-1}$ , as described by Golub and Kahan (1965), we obtain an approximate solution for  $\mathbf{Z}'_\alpha$  as

$$\mathbf{Z}'_\alpha \approx M_\alpha^{-1} \mathbf{R}_\alpha. \quad (69)$$

## 4 | NUMERICAL SIMULATION OF GRAVITY WAVE-INDUCED TRACER TRANSPORT

We extend a gravity wave parameterization model to compute the previously discussed gravity wave tracer flux convergences. The model is coupled with a flow solver, both of which are introduced in Section 4.1. The treatment of leading-order and next-order flux convergences is detailed in Sections 4.2 and 4.3, respectively. To validate our approach, we compare parameterized gravity wave simulations at coarse resolution against high-resolution, wave-resolving reference simulations.

### 4.1 | Numerical Model

In the following section, we introduce the Pseudo-Incompressible Flow solver (PincFlow) used to simulate the resolved flow. PincFlow operates in two modes: a high-resolution, wave-resolving mode for generating reference data and a low-resolution mode with parameterized gravity waves, incorporating a Lagrangian ray tracer. We then present the gravity wave model, which computes the gravity wave impact on the resolved flow and is couple to PincFlow.

#### 4.1.1 | PincFlow

PincFlow solves the pseudo-incompressible equations, first introduced by (Durran, 1989), in conservative flux form, as presented by Klein (2009), Rieper et al. (2013), Schmid et al. (2021), and Jochum et al. (2025). The model includes a passive tracer mixing ratio,  $\psi$ , whose transport is described by Equation (1) and, in flux form, by

$$\frac{\partial(\rho\psi)}{\partial t} + \nabla \cdot (\rho\psi\mathbf{v}) = 0. \quad (70)$$

Atmospheric variables are discretized on a C-grid (Arakawa and Lamb, 1977), where density, Exner pressure, and tracer mixing ratio are defined at cell centers, while the wind components  $u$ ,  $v$ , and  $w$  are staggered along the  $x$ -,  $y$ -, and  $z$ -directions, respectively. Mass, tracer, and momentum fluxes are computed using a monotone upwind scheme (van Leer, 1979). The equations are integrated using a semi-implicit time-stepping scheme (Schmid et al., 2021). The tracer advection equation (Equation (70)) is solved explicitly twice per time step, each over half a step. For explicit time integration, the third-order Runge-Kutta method of Williamson (1980) is employed.

#### 4.1.2 | PincFlow/MS-GWaM

For coarse-resolution simulations using PincFlow, the gravity wave impact on the large-scale flow can be parameterized with the Multi-Scale Gravity-Wave Model (MS-GWaM). The modeled gravity waves are represented by a spectral extension of the WKB theory (Achatz et al., 2023) and integrates it using a Lagrangian approach. Below, we provide a brief overview of MS-GWaM, while more detailed descriptions can be found in Muraschko et al. (2015), Böllöni et al. (2016), Wilhelm et al. (2018), Wei et al. (2019), and Jochum et al. (2025).

MS-GWaM calculates the propagation of phase-space (or spectral) wave action density  $\mathcal{N}$ , where

$$\mathcal{N}(\mathbf{x}, \mathbf{k}, t) = \sum_{\alpha=1}^M \mathcal{A}_{\alpha}(\mathbf{x}, t) \delta[\mathbf{k} - \mathbf{k}_{\alpha}(\mathbf{x}, t)], \quad (71)$$

using the conservation equation

$$\frac{d\mathcal{N}}{dt} \equiv \frac{\partial \mathcal{N}}{\partial t} + \mathbf{c}_g \cdot \nabla_{\mathbf{x}} \mathcal{N} + \dot{\mathbf{k}} \cdot \nabla_{\mathbf{k}} \mathcal{N} = 0, \quad (72)$$

meaning  $\mathcal{N}$  is conserved along ray trajectories. These trajectories are defined by the group velocity and rate of change of wavenumber

$$\frac{d\mathbf{x}}{dt} = \mathbf{c}_g = \nabla_{\mathbf{k}} \Omega, \quad (73)$$

$$\frac{d\mathbf{k}}{dt} = \dot{\mathbf{k}} = -\nabla_{\mathbf{x}} \Omega, \quad (74)$$

respectively, where

$$\Omega(\mathbf{x}, \mathbf{k}, t) = \mathbf{k}_h \cdot \langle \mathbf{u} \rangle(\mathbf{x}, t) \pm \sqrt{\frac{k_h^2 N^2(z) + f^2 m^2}{k_h^2 + m^2}} \quad (75)$$

represents the gravity-wave dispersion relation.

Numerically, the problem is discretized by dividing phase-space regions with nonzero wave action density into six-dimensional cuboid ray volumes, extending in the  $x$ -,  $y$ -,  $z$ -,  $k$ -,  $l$ -, and  $m$ -directions. Since the phase-space velocity is divergence-free:

$$\nabla_{\mathbf{x}} \cdot \mathbf{c}_g + \nabla_{\mathbf{k}} \cdot \dot{\mathbf{k}} = 0, \quad (76)$$

the volume content of each ray remains constant during propagation. While ray volumes maintain their cuboid shape—meaning shear effects are only captured by subdividing sheared regions—they can stretch or compress in a volume-preserving manner.

In the next-two sections, we extend MS-GWaM to calculate the leading- and next-order gravity wave tracer flux convergences, as discussed in Sections 2 and 3. To validate these extensions, we use two test cases of gravity wave packets, each designed so that one of the flux convergences dominates the gravity wave forcing on the large-scale tracer.

## 4.2 | Parameterization of the Leading-order Gravity Wave Tracer Flux Convergence

In this section, we present the parameterization of the leading-order gravity wave tracer flux convergence using MS-GWaM. To validate this extension, we simulate a three-dimensional gravity wave packet propagating through a large-scale tracer field that initially varies only in the vertical direction. We then compare the resulting changes in the large-scale tracer distribution with those from a wave-resolving reference simulation.

To adapt the theory described above to the spectral Lagrangian approach of MS-GWaM, we rewrite the leading-order flux convergence in terms of  $\mathcal{N}$ . From Equation (65), we obtain

$$Q^{(0)} = -\frac{1}{\bar{\rho}} \nabla \cdot \int d^3k \frac{f}{\bar{\omega}} \frac{m\mathcal{N}}{k_h^2 + m^2} (\mathbf{k} \times \nabla \psi). \quad (77)$$

It is important to note that the derivation of Equation (72) assumes geostrophic and hydrostatic equilibrium of the

large-scale flow to ensure the numerical feasibility of simulation  $\mathcal{N}$ , as presented in Achatz et al. (2023). However, this assumption is not required for the derivation of  $Q^{(0)}$  or  $Q^{(1)}$ . The geostrophic and hydrostatic equilibrium approximation introduces an  $O(\varepsilon)$  error in the prognostic equation (72) for  $\mathcal{N}$ . As demonstrated by Bölöni et al. (2016), Wei et al. (2019), and Jochum et al. (2025), and as will be confirmed by the following simulation results, this error appears to be sufficiently small for the predicted  $\mathcal{N}$  to yield reliable results.

The impact of gravity waves on tracer transport is incorporated by extending Equation (70) to

$$\frac{\partial(\rho\psi)}{\partial t} + \nabla \cdot (\rho\psi\mathbf{v}) = \rho Q^{(0)}. \quad (78)$$

While Equation (70) is used in wave-resolving reference simulations, the extend form, Equation (78), is applied when the model resolution is coarse and gravity waves are parameterized using MS-GWaM.

To validate the extension of PincFlow/MS-GWaM with Equations (77) and (78), we conduct three simulations of a three-dimensional gravity wave packet. A high-resolution wave-resolving simulation serves as our reference and will be referred to as 3DWR. To ensure the gravity wave is well resolved, we use at least 16 grid points per initial wavelength in each horizontal direction and 10 grid points per wavelength in the vertical direction. Additionally, we perform a coarse-resolution where the resolution is approximately one grid point per wavelength. Since the gravity wave impact, including  $Q^{(0)}$ , is not resolved at this resolution, it is parameterized using MS-GWaM. We denote this simulation as 3DCR. Finally, to assess the effect of the tracer flux convergence in Equation (78), we conduct another simulation with parameterized waves, but with  $Q^{(0)}$  neglected. This simulation is referred to as 3DCRno.

The atmosphere in the simulations is initialized as follows: We begin with a rotating, isothermal atmosphere at rest, with a temperature of  $T_0 = 300\text{K}$ . A locally monochromatic wave packet is introduced, where the atmospheric variables are given by

$$\mathbf{v} = \mathbf{v}', \quad (79)$$

$$\theta = \bar{\theta} + \theta', \quad (80)$$

$$\psi = \langle \psi \rangle + \psi'. \quad (81)$$

The potential temperature perturbation is initialized via the buoyancy using the WKB ansatz

$$\theta' = \frac{\bar{\theta}}{g} b'(\mathbf{x}, t) = \frac{\bar{\theta}}{g} \Re \left[ \hat{b}(\mathbf{x}, t) e^{i(l_0 y + m_0 z)} \right], \quad (82)$$

with wave amplitude  $\hat{b}$  and initial wavenumbers  $l_0$  and  $m_0$  in the  $y$ - and  $z$ -directions, respectively. The initial perturbations in the wind  $\mathbf{v}'$  and tracer mixing ration  $\psi'$  are determined from  $b'$  using the polarization relations (Equations (17), (28) and (29)). The buoyancy wave amplitude is initially defined by a Gaussian function in the  $z$ -direction and a cosine function in the  $x$ -direction, with no dependence on  $y$ :

$$\hat{b}(\mathbf{x}, t = 0) = a_0 \frac{N^2}{m_0^2} \exp \left[ -\frac{(z - z_0)^2}{2\sigma_z^2} \right] \begin{cases} \cos \left[ \frac{\pi(x - x_0)}{2\sigma_x} \right] & \text{for } |x - x_0| \leq \sigma_x, \\ 0 & \text{else,} \end{cases} \quad (83)$$

where  $(x_0, z_0)$  is the position of the wave amplitude maximum in the  $x$ - $z$ -plane, while  $\sigma_x$  and  $\sigma_z$  define the width of the wave packet in the  $x$ - and  $z$ -directions, respectively. The initial vertical wavenumber  $m_0$  is chosen such that  $m_0 < 0$ , ensuring the wave packet propagates upwards when selecting the positive branch of the intrinsic frequency

and setting  $k_0 > 0$ . The factor  $a_0$  scales the buoyancy amplitude relative to the threshold of static instability, which is reached at  $a_0 = 1$ . Additionally, the initial large-scale tracer distribution  $\langle \psi \rangle$  is prescribed as a linear function of altitude:

$$\langle \psi \rangle (t = 0) = \alpha_\psi z, \quad (84)$$

where  $\alpha_\psi$  is an arbitrary scaling parameter. All simulation parameters are summarized in Table 2.

In the coarse-resolution simulations 3DCR and 3DCRno, the large-scale tracer distribution  $\langle \psi \rangle$  and velocity  $\langle \mathbf{v} \rangle$  are obtained directly as output. However, in the high-resolution wave-resolving simulation 3DWR, the output consists of the full variables  $\psi$  and  $\mathbf{v}$ , which include both the large-scale and gravity wave components. Therefore, post-processing is required to extract  $\langle \psi \rangle$  and  $\langle \mathbf{v} \rangle$ . Since the initial wave packet setup in Equation (83) assumes no dependence on the  $y$ -coordinate for the large-scale variables, we can extract them by averaging the full variables over one wavelength in the  $y$ -direction. The gravity wave components are then determined as

$$\psi' = \psi - \langle \psi \rangle, \quad (85)$$

$$\mathbf{v}' = \mathbf{v} - \langle \mathbf{v} \rangle. \quad (86)$$

This enables us to compute the leading-order gravity wave tracer flux convergence

$$Q^{(0)} = -\frac{1}{\bar{\rho}} \nabla \cdot \langle \bar{\rho} \mathbf{v}' \psi' \rangle, \quad (87)$$

which we can then compare to the  $Q^{(0)}$  obtained from MS-GWaM.

The results after 1500 min are visualized in Figure 1, showing the gravity wave tracer flux convergence  $Q^{(0)}$  and the resulting change in the tracer distribution for 3DWR, 3DCR, and 3DCRno. In the reference simulation 3DWR, the gravity wave packet leads to a decrease in the tracer mixing ratio to the left and an increase to the right of the wave packet amplitude maximum. This behaviour can be explained by the initial setup of  $\mathbf{k}_0 = (0, l_0, m_0)$  and  $\nabla \langle \psi \rangle = \alpha_\psi \mathbf{e}_z$ , as the wave packet has changed only slightly during the 1500-minute simulation due to its relatively small vertical group velocity. Comparing 3DCR to the reference simulation 3DWR, we find that the fluxes and the resulting changes in the large-scale tracer distribution are well reproduced. To assess the effect of setting  $Q^{(0)} = 0$ , we compare 3DCR to 3DCRno, where the latter neglects  $Q^{(0)}$ . In 3DCRno, the large-scale tracer  $\langle \psi \rangle$  is only advected by the wave-induced large-scale wind (not shown). The resulting  $\Delta \langle \psi \rangle$  differs significantly from that in 3DCR, and consequently from 3DWR. Thus, we conclude that the changes in  $\Delta \langle \psi \rangle$  observed in 3DWR and 3DCR are significantly impacted by  $Q^{(0)}$  and not merely a result of advection due to the large-scale wind  $\langle \mathbf{v} \rangle$ .

### 4.3 | Parameterization of the Next-order Gravity Wave Tracer Flux Convergence

In the following, we present the extension of MS-GWaM to calculate the next-order flux convergence  $Q^{(1)}$ . To validate this extension, we conduct simulations of a vertically propagating, two-dimensional, locally monochromatic gravity wave packet in an isothermal, non-rotating atmosphere. The absence of rotation in the atmosphere ensures that there are no leading-order effect induced by inertial gravity waves.

From the extension of MS-GWaM to calculate  $Q^{(1)}$ , we assume a locally monochromatic wave packet. Dropping

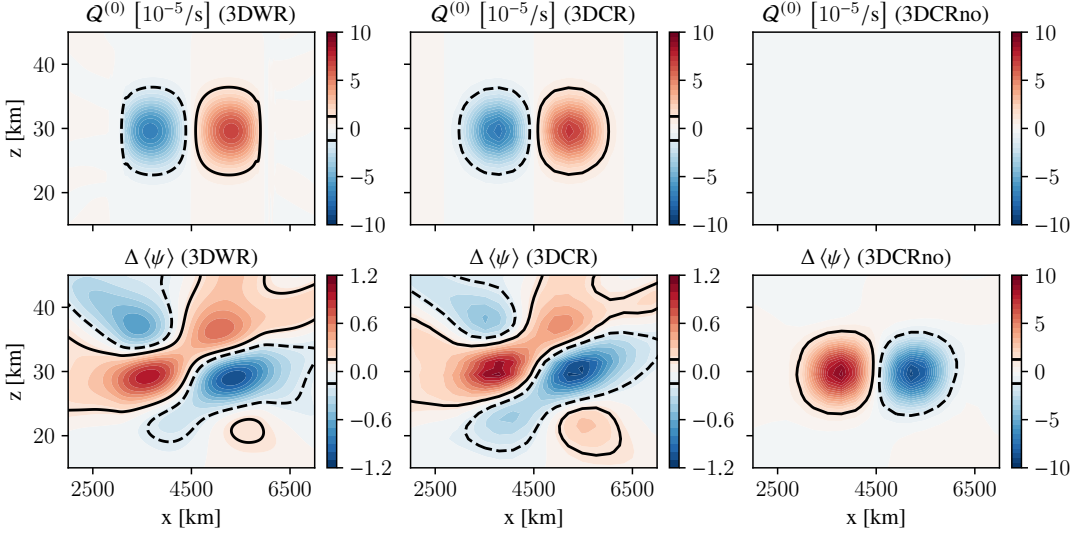


**FIGURE 1** Gravity wave-induced tracer flux convergence  $Q^{(0)}$  (top row) and change in the large-scale tracer distribution  $\Delta \langle \psi \rangle$  (bottom row) from a three-dimensional gravity wave packet, at  $t = 1500\text{min}$ ; (left column) 3DWR: wave-resolving reference simulation; (center column) 3DCR: coarse-resolution simulation with parameterized gravity wave and including  $Q^{(0)}$ ; (right column) 3DCRno: coarse-resolution simulation with  $Q^{(0)} = 0$ . The solid and dashed contour lines illustrate the regions with positive and negative values, respectively.

the index  $\alpha$  from the equations summarized in Section 3, the wave energy is given

$$E_w = \bar{\rho} \frac{|\hat{b}|^2}{2N^2} \frac{\hat{\omega}^2 (k_h^2 + m^2)}{N^2 k_h^2} = \int d^3k \hat{\omega} N, \quad (88)$$

and we can therefore determine the absolute magnitude of the buoyancy

$$|\hat{b}| = \left[ \int d^3k \frac{N}{\bar{\rho}} \frac{2N^4 k_h^2}{\hat{\omega} (k_h^2 + m^2)} \right]^{1/2}. \quad (89)$$

Within MS-GWaM, the wavenumber integral is calculated by summing the contributions from all ray volumes within a PincFlow finite volume cell. As discussed in Section 2, we can determine both the leading- and next-order wave amplitudes from the buoyancy amplitude  $\hat{b} = |\hat{b}| e^{i\Lambda}$ , allowing us to parameterize the next-order tracer flux convergence. Numerically, all required temporal and spatial derivatives are approximated using simple finite differences. It is important to note that in the present monochromatic case, Equation (68) predicts that the large-scale phase remains invariant.

The tracer transport equation is thus extended to

$$\frac{\partial(\rho\psi)}{\partial t} + \nabla \cdot (\rho\psi\mathbf{v}) = \rho Q^{(1)}, \quad (90)$$

where Equation (90) is used in coarse-resolution simulations with parameterized gravity waves through MS-GWaM,



while wave-resolving simulations solve Equation (70).

We conduct a wave-resolving simulation (2DWR) as a reference simulation and a simulation with parameterized gravity waves (2DCR). To emphasize the impact of  $Q^{(1)}$ , we also conduct an additional coarse-resolution simulation with parameterized waves where we set  $Q^{(1)} = 0$  (2DCRno). In the case of 2DWR, the resolution is 16 grid points per wavelength in the  $x$ -direction and 10 grid points per vertical wavelength in the  $z$ -direction. For 2DCR and 2DCRno, we choose one grid point per wavelength in both the horizontal and vertical directions.

We initialize the isothermal atmosphere ( $T_0 = 300\text{K}$ ) with a two-dimensional wave packet, where the buoyancy amplitude depends only on altitude and is given by a Gaussian function,

$$\hat{b} = a_0 \frac{N^2}{m_0^2} \exp \left[ -\frac{(z - z_0)^2}{2\sigma^2} \right]. \quad (91)$$

The buoyancy perturbation  $b'$  is therefore

$$b' = \text{Re} \left[ \hat{b} e^{i(k_0 x + m_0 z)} \right], \quad (92)$$

from which all remaining perturbations in the atmospheric variables are calculated using the polarization relations. Since the wave packet is meant to propagate upwards, we select the positive branch of the frequency with  $k_0 > 0$  and  $m_0 < 0$  for the horizontal and vertical wavenumbers, respectively. As we are interested only in the second-order gravity wave effects, and not in turbulent mixing induced by breaking gravity waves, we set  $a_0 = 0.1$  so that the gravity wave packet remains far from static instability throughout the simulation. The initial large-scale tracer distribution is linearly increasing with altitude, as given in Equation (84).

We calculate the large-scale variables from the 2DWR results by averaging over one wavelength in the horizontal direction. From there, we can calculate the perturbations in the atmospheric variables, as given in Equations (85) and (86). Using these, we can then calculate the tracer flux convergence

$$Q^{(1)} = \frac{1}{\bar{\rho}} \frac{\partial}{\partial z} \langle \bar{\rho} w' \psi' \rangle. \quad (93)$$

As the atmosphere is not rotating, we can be sure that there are no effects due to leading-order fluxes, as those are of an inertial nature.

The results of 2DWR, 2DCR, and 2DCRno over a simulation time of 60 min are visualized in Figure 2. Both the next-order tracer flux convergence  $Q^{(1)}$  and the change in the large-scale tracer distribution calculated in 2DWR are replicated by the parameterized gravity wave simulation. We observe that the gravity wave causes a vertical tracer flux towards the center of the wave packet. In the case of 2DCRno, where  $Q^{(1)} = 0$ , we observe no change in the large-scale tracer distribution, as there is no large-scale vertical wind (not shown). We can therefore conclude that the  $\Delta \langle \psi \rangle$  seen in the results for 2DWR and 2DCR are accurately parameterized in 2DCR.

## 5 | SUMMARY AND CONCLUSIONS

While the large-scale zonal-averaged transport of tracers is characterized by global circulations and well resolved in weather and climate models, the effect of small-scale processes, such as gravity waves must be parameterized. Therefore, this study investigates the impact of small-scale gravity waves on large-scale tracer transport and presents how this impact can be calculated within a gravity wave parameterization model. We employ a multiple-scale analysis

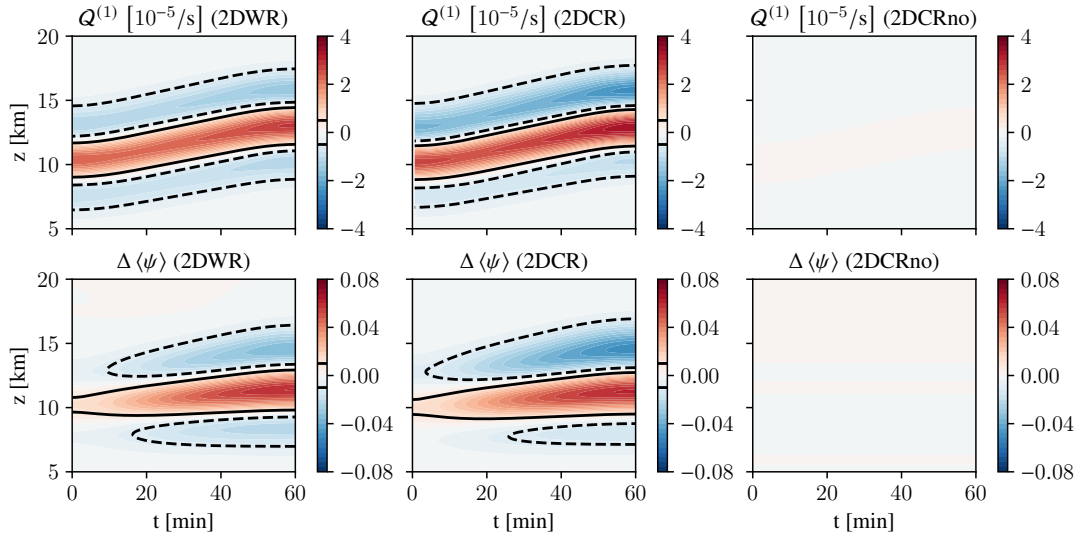


**FIGURE 2** Time evolution of the gravity wave-induced tracer flux convergence  $Q^{(1)}$  (top row) and change in the large-scale tracer distribution  $\Delta \langle \psi \rangle$  (bottom row) from a two-dimensional gravity wave packet; (left column) 2DWR: wave-resolving reference simulation; (center column) 2DCR: coarse-resolution simulation with parameterized gravity wave and including  $Q^{(1)}$ ; (right column) 2DCRno: coarse-resolution simulation with  $Q^{(1)} = 0$ . The solid and dashed contour lines illustrate the regions with positive and negative values, respectively.

of the governing equations, assuming that the large-scale flow and wave amplitudes vary slowly in space and time compared to the rapid fluctuations of gravity waves. The analysis relied on the scale separation parameter  $\varepsilon$ , utilizing the WKB ansatz to describe gravity waves and systematically expanding the equations in powers of  $\varepsilon$ . Sorting the resulting equations by their orders in  $\varepsilon$  enabled the identification of the most significant impacts of gravity waves on tracer transport.

Our findings reveal the leading-order and next-order contributions of small-scale gravity waves to large-scale tracer transport. The leading-order impact, induced by inertial gravity waves, acts perpendicular to both the large-scale tracer gradient and the wave number. The next-order impact becomes particularly significant at lower latitudes, where the Coriolis parameter becomes small and therefore also the leading-order impact, due to its non-zero contribution in the absence of rotation. These impacts scale as  $\mathcal{O}(\varepsilon^{2\gamma+1})$  and  $\mathcal{O}(\varepsilon^{2\gamma+2})$ , respectively, when compared to the large-scale wind advection ( $\mathcal{O}(1)$ ), with  $\gamma = 0, 1, 2$  corresponding to large-amplitude, weakly nonlinear, and quasi-linear waves. Additionally, we demonstrated that gravity wave effects can be calculated from the leading-order buoyancy amplitude and gravity wave energy. We extended a gravity wave parameterization model to calculate these effects. Validation of these results was performed using two idealized wave packet test cases, where comparisons with wave-resolving reference simulations confirmed the accuracy of the approach.

These findings enable highly accurate simulations of tracer transport that incorporate gravity wave effects without the computational cost of resolving the waves explicitly. This work represents an important step toward a comprehensive understanding of the small-scale non-chemical processes that perturb tracer distributions. To build on this foundation, future research should aim to include the effects of diffusive mixing due to turbulence, such as that caused by breaking gravity waves.

## Acknowledgements

I. K. and U. A. thank the German Research Foundation (DFG) for partial support through CRC 301 “TPChange” (Project No. 428312742 and Projects B06 “Impact of small-scale dynamics on UTLS transport and mixing,” B07 “Impact of cirrus clouds on tropopause structure,” and Z03 “Joint model development and modelling synthesis”). U. A. thanks the German Research Foundation (DFG) for partial support through the CRC 181 “Energy transfers in Atmosphere and Ocean” (Project No. 274762653 and Projects W01 “Gravity-wave parameterization for the atmosphere” and S02 “Improved Parameterizations and Numerics in Climate Models”).

## Data statement

The code and data described in this study are available on request.

## Conflict of interest

The authors declare no conflicts of interest.

## References

- Achatz, U., Kim, Y.-H. and Voelker, G. S. (2023) Multi-scale dynamics of the interaction between waves and mean flows: From nonlinear WKB theory to gravity-wave parameterizations in weather and climate models. *Journal of Mathematical Physics*, **64**.
- Achatz, U., Klein, R. and Senf, F. (2010) Gravity waves, scale asymptotics and the pseudo-incompressible equations. *Journal of Fluid Mechanics*, **663**, 120–147.
- Achatz, U., Ribstein, B., Senf, F. and Klein, R. (2017) The interaction between synoptic-scale balanced flow and a finite-amplitude mesoscale wave field throughout all atmospheric layers: weak and moderately strong stratification. *Quarterly Journal of the Royal Meteorological Society*, **143**, 342–361.
- Arakawa, A. and Lamb, V. R. (1977) Computational Design of the Basic Dynamical Processes of the UCLA General Circulation Model. In *General Circulation Models of the Atmosphere* (ed. J. Chang), vol. 17 of *Methods in Computational Physics: Advances in Research and Applications*, 173–265. Elsevier.
- Brewer, A. W. (1949) Evidence for a world circulation provided by the measurements of helium and water vapour distribution in the stratosphere. *Quarterly Journal of the Royal Meteorological Society*, **75**, 351–363.
- Butchart, N. (2014) The Brewer-Dobson circulation. *Reviews of Geophysics*, **52**, 157–184.
- Böläni, G., Ribstein, B., Muraschko, J., Sgoff, C., Wei, J. and Achatz, U. (2016) The Interaction between Atmospheric Gravity Waves and Large-Scale Flows: An Efficient Description beyond the Nonacceleration Paradigm. *Journal of the Atmospheric Sciences*, **73**, 4833–4852.
- Dobson, G. M. B. (1956) Origin and distribution of the polyatomic molecules in the atmosphere. *Proceedings of the Royal Society of London. Series A. Mathematical and Physical Sciences*, **236**, 187–193.
- Durrán, D. R. (1989) Improving the Anelastic Approximation. *Journal of Atmospheric Sciences*, **46**, 1453–1461.
- Gardner, C. S., Guo, Y. and Liu, A. Z. (2019) Parameterizing Wave-Driven Vertical Constituent Transport in the Upper Atmosphere. *Earth and Space Science*, **6**, 904–913.

- Golub, G. and Kahan, W. (1965) Calculating the Singular Values and Pseudo-Inverse of a Matrix. *Journal of the Society for Industrial and Applied Mathematics Series B Numerical Analysis*, **2**, 205–224.
- Jochum, F., Chew, R., Lott, F., Voelker, G. S., Weinkaemmerer, J. and Achatz, U. (2025) The Impact of Transience in the Interaction between Orographic Gravity Waves and Mean Flow. *Journal of the Atmospheric Sciences*, **82**, 425 – 442.
- Klein, R. (2009) Asymptotics, structure, and integration of sound-proof atmospheric flow equations. *Theoretical and Computational Fluid Dynamics*, **23**, 161–195.
- Liu, A. Z. and Gardner, C. S. (2004) Vertical dynamical transport of mesospheric constituents by dissipating gravity waves. *Journal of Atmospheric and Solar-Terrestrial Physics*, **66**, 267–275.
- Muraschko, J., Fruman, M. D., Achatz, U., Hickel, S. and Toledo, Y. (2015) On the application of Wentzel-Kramer-Brillouin theory for the simulation of the weakly nonlinear dynamics of gravity waves. *Quarterly Journal of the Royal Meteorological Society*, **141**, 676–697.
- Rieper, F., Hickel, S. and Achatz, U. (2013) A Conservative Integration of the Pseudo-Incompressible Equations with Implicit Turbulence Parameterization. *Monthly Weather Review*, **141**, 861–886.
- Schmid, F., Gagarina, E., Klein, R. and Achatz, U. (2021) Toward a Numerical Laboratory for Investigations of Gravity Wave–Mean Flow Interactions in the Atmosphere. *Monthly Weather Review*, **149**, 4005–4026.
- van Leer, B. (1979) Towards the ultimate conservative difference scheme. V. A second-order sequel to Godunov's method. *Journal of Computational Physics*, **32**, 101–136.
- Walterscheid, R. L. and Schubert, G. (1989) Gravity wave fluxes of O<sub>3</sub> and OH at the nightside mesopause. *Geophysical Research Letters*, **16**, 719–722.
- Wei, J., Bölöni, G. and Achatz, U. (2019) Efficient Modeling of the Interaction of Mesoscale Gravity Waves with Unbalanced Large-Scale Flows: Pseudomomentum-Flux Convergence versus Direct Approach. *Journal of the Atmospheric Sciences*, **76**, 2715–2738.
- Wilhelm, J., Akylas, T. R., Bölöni, G., Wei, J., Ribstein, B., Klein, R. and Achatz, U. (2018) Interactions between mesoscale and submesoscale gravity waves and their efficient representation in mesoscale-resolving models. *Journal of the Atmospheric Sciences*, **75**, 2257–2280.
- Williamson, J. H. (1980) Low-storage Runge-Kutta schemes. *Journal of Computational Physics*, **35**, 48–56.
- Xu, J., Ma, R. and Smith, A. K. (2002) The study and applications of photochemical-dynamical gravity wave model II. *Science in China Series A: Mathematics*, **45**, 175–182.

**TABLE 2** Initial model parameters for the simulations of the three-dimensional wave packet (3D) and the two-dimensional wave packet (2D). The number of grid points  $N_x$ ,  $N_y$ , and  $N_z$  are given for the wave-resolving simulations (WR) and the coarse-resolution simulations with parameterized gravity waves (CR).

| Parameter  | 3D        | 2D   |
|--|-----------|------|
| Wavelength in $x$ -direction $\lambda_x$ [km]          | –         | 1    |
| Wavelength in $y$ -direction $\lambda_y$ [km]          | 300       | –    |
| Wavelength in $z$ -direction $\lambda_z$ [km]          | –1        | 1    |
| Branch of intrinsic frequency $\hat{\omega}$           | +1        | –1   |
| Wave amplitude factor $a_0$                            | 0.5       | 0.1  |
| Width of wave packet in $x$ -direction $\sigma_x$ [km] | 1500      | –    |
| Width of wave packet in $z$ -direction $\sigma_z$ [km] | 30        | 2    |
| Wave packet position in $x$ -direction $x_0$ [km]      | 4500      | –    |
| Wave packet position in $z$ -direction $z_0$ [km]      | 30        | 10   |
| Coriolis parameter $f$ [ $s^{-1}$ ]                    | $10^{-4}$ | 0    |
| Brunt-Vaisala frequency $N$ [ $s^{-1}$ ]               | 0.02      | 0.02 |
| Atmosphere temperature $T_0$ [K]                       | 300       | 300  |
| Tracer mixing ratio factor $\alpha_\psi$ [ $m^{-1}$ ]  | 1         | 1    |
| Domain size in $x$ -direction $L_x$ [km]               | 9000      | 1    |
| Domain size in $y$ -direction $L_y$ [km]               | 300       | –    |
| Domain size in $z$ -direction $L_z$ [km]               | 100       | 30   |
| Number of grid points in $x$ -direction (WR) $N_x$     | 512       | 32   |
| Number of grid points in $y$ -direction (WR) $N_y$     | 16        | –    |
| Number of grid points in $z$ -direction (WR) $N_z$     | 1000      | 960  |
| Number of grid points in $x$ -direction (CR) $N_x$     | 32        | 3    |
| Number of grid points in $y$ -direction (CR) $N_y$     | 1         | –    |
| Number of grid points in $z$ -direction (CR) $N_z$     | 100       | 300  |